Nuclear Physics B288 (1987) 681–716
North-Holland, Amsterdam

LARGE DEPARTURES FROM LANDAU DISTRIBUTIONS FOR HIGH-ENERGY PARTICLES TRAVERSING THIN Si AND Ge TARGETS

J.F. BAK, A. BURENKOV[1], J.B.B. PETERSEN and E. UGGERHØJ

Institute of Physics, University of Aarhus, DK-8000 Aarhus C, Denmark

S.P. MØLLER[2]

CERN, CH-1211 Genève 23, Switzerland

P. SIFFERT

Centre de Recherches Nucleaires, F-67037 Strasbourg, France

Received 8 December 1986

Energy losses of 2 and 8 GeV/c positive and negative electrons, pions and protons transmitted through 32–1040 μm thick germanium and silicon targets are measured using the targets as semiconductor detectors. The measured energy-loss distributions are well-reproduced by calculations when the binding of the target electrons is taken into account. In particular, the increasing width, up to twice as large as the width of the Landau distribution, and the decreasing most probable energy loss as a function of decreasing target thickness, agree with calculations. The same two quantities increase as a function of the relativistic $\beta\gamma$ for $\beta\gamma \gtrsim 4$ until a saturation is reached for very large values of $\beta\gamma$. The constancy of the Fermi plateau, the saturation value of the most probable energy loss, is confirmed to the one percent level for the considered $\beta\gamma$ values and thicknesses.

1. Introduction

The present work is concerned with the energy lost by high-energy charged particles when traversing solid matter. We shall only consider the ionization energy loss stemming from excitation and ionization of target atoms. Since the energy is lost in quanta, fluctuations in the energy loss will exist, and the energy-loss process is described by a distribution function.

Collisions are usually divided into "close" and "distant" collisions, with a dividing impact parameter of the order of the size of the atom. These names are of

---

[1] Visitor from Institute of Applied Physics, Minsk, USSR.

[2] Permanent address: Institute of Physics, University of Aarhus, DK-8000 Aarhus C, Denmark.

classical origin, since the impact parameter is not always well defined quantum-mechanically. In a quantum-mechanical treatment, the momentum transfer is used to classify the collisions, but the terms "close" and "distant" are still used in the sense that the impact parameter b is related to a momentum transfer q by the "uncertainty relation", $b \sim \hbar/q$.

In the classical impact parameter description, the average energy loss is roughly proportional to the logarithm of the ratio between the maximum and minimum impact parameter. The maximum impact parameter for distant collisions increases proportional to γ, and a logarithmic rise with γ of the energy loss is expected. For $\gamma \gg 1$ the maximum impact parameter is large compared to atomic dimensions, and in a dense material, the presence of atoms between the projectile and the interacting atom saturates the electromagnetic field in the medium due to the polarization of these atoms. This density effect results in a saturation of distant collisions. Another $\ln\gamma$ increase in the average energy loss exists due to the increase in the maximum energy transfer with γ. This maximum energy transfer, however, does not influence the most probable energy loss, which is only dependent on distant collisions and saturates at the so-called Fermi plateau at high values of γ.

The energy-loss distribution for relativistic particles is given by a gaussian-like function with a high-energy tail, stemming from large, but infrequent, energy transfers from close collisions. When the energy loss is very large compared to the binding energy of the target electrons, the width of the distribution is only dependent on the number of electrons and not on their binding energy. The distribution function is then given by the Landau function. For thin targets, where the energy loss is comparable to or smaller than the binding energy of inner-shell electrons, the energy-loss distribution is broader than when the electronic binding energy is neglected.

The present investigations are concerned precisely with this region of thicknesses, and the electronic binding energies have to be taken into account. In thin targets the reduction of the projectile energy when traversing the target cannot be measured directly, because the energy loss is extremely small compared to the projectile energy. However, when the target is a semiconductor detector, the energy deposited in the target can be measured, and this deposited energy loss is in fact closely related to the energy loss. The experiments have thus been restricted to silicon and germanium targets.

This work is in part motivated by earlier work, where a broadening of the energy-loss distribution was observed [23], and in part by the increasing use of thin semiconductor detectors in high-energy physics for the detection of relativistic particles. These detectors are used mainly as position-sensitive (strip or CCD) detectors, often as active, "live", targets. The strip detectors have thicknesses of a few hundred microns, whereas the CCD detectors are very thin (some tens of microns). Although much work, both theoretical and experimental, has been made for gaseous targets (see, e.g., ref. [3] and references therein), very few investigations have been performed for solid targets. A theoretical discussion, sect. 2, giving the necessary outline of the theory, is followed by a discussion of the experimental procedure in sect. 3. The experimental results are presented in sect. 4, which also contains the discussion and the comparison with the model calculations.

2. Theory

In this section the models are discussed with which the experimental results are compared. Normally the energy loss of relativistic particles is calculated quantum-mechanically, resulting in the Bethe formula with various corrections, see, e.g., ref. [1]. An energy-loss cross section which is needed to calculate the energy-loss distribution is, however, not easily obtained from this formulation. So a semiclassical calculation is set up starting with a simple model for the energy-loss cross section. This calculation gives the same average energy loss as the Bethe formula.

2.1. SEMICLASSICAL ENERGY LOSS CALCULATION

In this model [2, 3] the target material is treated as a homogeneous, isotropic medium with electromagnetic properties described by a dielectric function ε. The mean energy loss per unit path length is found as the effect of the electric field, $\boldsymbol{E}$, set up in the medium due to the presence of the charged projectile moving with velocity $v = \beta c$. This field exerts work on the projectile giving

$$-\frac{\mathrm{d}E}{\mathrm{d}x} = -\frac{e\boldsymbol{E}(\boldsymbol{\beta}ct, t)\cdot\boldsymbol{\beta}}{\beta}. \tag{1}$$

This can be rewritten by solving Maxwell's equations for the Fourier transformed fields

$$-\frac{\mathrm{d}E}{\mathrm{d}x} = -\frac{e^2 i}{\beta^2 \pi}\int_{-\infty}^{\infty}\omega\,\mathrm{d}\omega\int_{|\omega|/v}^{\infty}k\,\mathrm{d}k\left[\frac{\omega/k^2c^2-\beta^2}{\varepsilon\omega^2-k^2c^2}-\frac{1}{k^2c^2\varepsilon}\right]. \tag{2}$$

Now $\varepsilon = \varepsilon(k, \omega)$, and the Fourier variables ω and k are interpreted as the energy and momentum transfer, in units of $\hbar$. The first term describes transverse excitations and the second longitudinal ones. In general the dielectric function for transverse and longitudinal excitations entering the first and the second term in eq. (2), respectively, differ [4]. However in non-magnetic materials, they coincide. In any case significant contributions to the transverse term only comes from $\varepsilon\omega^2 \simeq k^2c^2$, i.e. in a narrow region above the lower integration limit. For the free electron gas and high projectile velocities the longitudinal and the transverse dielectric function are almost equal in this region. Furthermore, for these small k-values the dipole approximation is valid and we set $\varepsilon(\omega, k) = \varepsilon(\omega, 0) \equiv \varepsilon(\omega)$ in the integration of the first term, and obtain the result for the transverse contribution

$$-\left(\frac{\mathrm{d}E}{\mathrm{d}x}\right)_{\perp}=\frac{e^2}{\pi v^2}\left\{\int_0^{\infty}\omega\,\mathrm{d}\omega\,\mathrm{Im}\left[-\frac{1}{\varepsilon(\omega)}\right]\ln\frac{\gamma^2\omega^2}{(\omega^2+l^2)}+\frac{l^2}{\omega_{\mathrm{p}}^2\gamma^2}-\beta^2\right\} \tag{3}$$

where l is the single root of the equation

$$1-\beta^2\varepsilon(il)=0. \tag{4}$$

As will be seen later, l determines the density effect. When $1-\beta^2\varepsilon(0)\geq 0$, there is no density effect, $l=0$. Also the longitudinal contribution can be expressed in terms of $\mathrm{Im}(1/\varepsilon)$

$$-\left(\frac{\mathrm{d}E}{\mathrm{d}x}\right)_{\parallel}=\frac{2e^2}{\pi v^2}\int_0^{\infty}\omega\,\mathrm{d}\omega\int_{\omega/v}^{\infty}\frac{\mathrm{d}k}{k}\mathrm{Im}\left(\frac{-1}{\varepsilon(k,\omega)}\right) \tag{5}$$

but to perform the k-integration a model for $\varepsilon(k,\omega)$ is needed. It is though, possible to integrate the above equation [2] by first integrating over ω at constant k, by using the sum rule

$$\int_0^{\infty}\omega\,\mathrm{d}\omega\,\mathrm{Im}(-1/\varepsilon)=\tfrac{1}{2}\pi\omega_{\mathrm{p}}^2. \tag{6}$$

However, since we shall need to quantize our expression for the energy loss, when integrated over k, to get an energy-loss cross section, a model for $\varepsilon(k,\omega)$ is introduced.

We will write

$$\mathrm{Im}\left(-\frac{1}{\varepsilon(k,\omega)}\right)=\frac{\pi}{2}\frac{\omega_{\mathrm{p}}^2}{\omega}\sum_n F_n\delta(\omega-\Omega_n(k)), \tag{7}$$

with

$$\Omega_n(k)=\begin{cases}\Omega_{0n} & \text{for } k\leq\sqrt{2m\Omega_{0n}/\hbar}\\ \hbar^2k^2/2m & \text{for } k\geq\sqrt{2m\Omega_{0n}/\hbar}\,.\end{cases} \tag{8}$$

The solid is thus represented as a set of oscillators with an excitation frequency spectrum given by $\Omega_n(k)$, with only one bound state Ω_{0n} for each atomic shell. For energy transfers larger than Ω_{0n} the atomic electron is treated as free. A discussion of the choice of Ω_{0n} will be given later. The dipole oscillator strengths F_n will be approximated by $F_n=q_n/Z$, where q_n is the number of electrons pertaining to the nth shell, and Z the atomic number. The expression for $\mathrm{Im}(-1/\varepsilon)$ is normalized so that the sum rule (6) is fulfilled. The condition for setting $\varepsilon(k,\omega)=\varepsilon(0,\omega)$ can now be formulated as $\hbar\Omega_{0n} \ll mc^2$; in other words, the target electrons must not be relativistic.

With this model we get for the total energy loss

$$-\frac{\mathrm{d}E}{\mathrm{d}x} = \frac{e^2\omega_\mathrm{p}^2}{2v^2}\sum_n F_n\left\{\int_{\Omega_{0n}}^{\infty}\mathrm{d}\omega\left[\delta(\omega-\Omega_{0n})\ln\frac{2mc^2\beta^2\gamma^2\omega}{\hbar(\omega^2+l^2)}+\frac{1}{\omega}\right]+\frac{l^2}{\omega_\mathrm{p}^2\gamma^2}-\beta^2\right\}, \quad (9)$$

which can be integrated over ω to give

$$-\frac{\mathrm{d}E}{\mathrm{d}x} = \frac{e^2\omega_\mathrm{p}^2}{2v^2}\left[\sum_n F_n\ln\frac{2mc^2\beta^2\gamma^2E_\mathrm{max}}{E_{0n}^2+\hbar^2l^2}+\frac{l^2}{\omega_\mathrm{p}^2\gamma^2}-\beta^2\right], \quad (10)$$

where $E_\mathrm{max} = \hbar\omega_\mathrm{max} \approx 2mc^2\beta^2\gamma^2$ is the maximum energy transfer, and $E_{0n} = \hbar\Omega_{0n}$. It will suffice to use this approximate expression for E_max, since the main interest is the most probable energy loss, uninfluenced by the very close collisions. The dielectric function is given by (damping negligible)

$$\varepsilon(\omega) = 1-\omega_\mathrm{p}^2\sum_n\frac{f_n}{\omega^2-\omega_n^2}, \quad (11)$$

consistent with the model for $\mathrm{Im}(1/\varepsilon)$, where to a good approximation [5] $f_n = F_n$ and $\Omega_{0n}^2 = \omega_n^2+\omega_\mathrm{p}^2f_n$. The equation determining the density effect is then

$$\omega_\mathrm{p}^2\sum_n\frac{f_n}{l^2+\omega_n^2} = \frac{1}{\beta^2\gamma^2}, \quad (12)$$

with asymptotic solutions

$$l^2 = 0 \qquad \text{for } \beta\gamma \ll \omega_n/\omega_\mathrm{p},$$

$$l^2 = \omega_\mathrm{p}^2\beta^2\gamma^2 \qquad \text{for } \beta\gamma \gg \omega_n/\omega_\mathrm{p}, \quad (13)$$

giving for the energy loss

$$-\frac{\mathrm{d}E}{\mathrm{d}x} = \frac{e^2\omega_\mathrm{p}^2}{2v^2}\left[\ln\frac{2mc^2\beta^2\gamma^2E_\mathrm{max}}{I^2}-\beta^2\right], \qquad \beta\gamma \ll \omega_n/\omega_\mathrm{p}, \quad (14)$$

$$-\frac{\mathrm{d}E}{\mathrm{d}x} = \frac{e^2\omega_\mathrm{p}^2}{2v^2}\ln\frac{2mc^2E_\mathrm{max}}{\hbar^2\omega_\mathrm{p}^2}, \qquad \beta\gamma \gg \omega_n/\omega_\mathrm{p}, \quad (15)$$

corresponding to the Bethe formula without density effect (14) and with full saturation of the transverse excitations (15). The average energy loss is often given as eq. (14) minus the density-effect correction δ, which is then the difference between eq. (10) and eq. (14). The density-effect correction has been evaluated by Sternheimer [5,18] for most substances. The mean ionization potential in the present model is given by

$$\ln I = \sum_n F_n \ln \hbar\Omega_{n0}. \tag{16}$$

For a restricted energy loss or the most probable energy loss, $E_{\max}$ is independent of γ (subsect. 2.5), and formula (15) is independent of γ giving the Fermi plateau for the saturated energy loss.

2.2. CALCULATION OF ENERGY-LOSS DISTRIBUTIONS

The energy loss calculated above is the average of the energy losses from many different projectile-target atom collisions, ranging from soft excitations of outer shell electrons to hard collisions producing δ-rays. The statistical nature of these collisions lead to fluctuations, straggling, in the energy lost by particles penetrating the target. We shall only consider targets of thickness x, so thin that the energy lost is much less than the projectile energy. The stopping power can thus be assumed constant during the passage. Let us introduce

$$\xi = \frac{2\pi e^4}{mc^2\beta^2} xNZ \tag{17}$$

as a measure of a typical energy loss (for Si: $\xi = 17.81$ [keV/mm] x/β^2). The decisive parameter determining the shape of the energy-loss distribution is $\kappa = \xi/E_{\max}$. For $\kappa \gg 1$, there is a sufficiently large number of large energy transfers, that the distribution is gaussian. Assuming $\xi \gg E_K$, where E_K is an atomic binding energy, Landau [6] solved the problem for $\kappa \ll 1$ in 1944.

The unknown distribution function is the solution of the kinetic equation, as formulated by Landau,

$$\frac{\partial f(x,\Delta)}{\partial x} = \int_0^\infty w(E)[f(x,\Delta - E) - f(x,\Delta)]\,\mathrm{d}E, \tag{18}$$

which defines $f(x,\Delta)$, once the collision probability (per unit length) $w(E) = N\mathrm{d}\sigma/\mathrm{d}E$ is given. Here $f(x,\Delta)\mathrm{d}\Delta$ is the probability for the projectile to have lost the energy Δ after traversing a target of thickness x. The distribution function is normalized, so that $\int f(x,\Delta)\mathrm{d}\Delta = 1$. The above integral is finite due to a finite maximum energy transfer $E_{\max}$ and a non-zero minimum energy transfer. The above kinetic equation can be solved by applying the Laplace transformation, given by

$$\varphi(x, p)=\int_0^{\infty} f(x, \Delta) \mathrm{e}^{-p \Delta} \mathrm{d} \Delta . \tag{19}$$

The inverse Laplace transformation is

$$f(x, \Delta)=\frac{1}{2 \pi i} \int_{-i \infty+\sigma}^{+i \infty+\sigma} \varphi(x, p) \mathrm{e}^{p \Delta} \mathrm{d} p, \quad \sigma>0 . \tag{20}$$

After Laplace transformation the kinetic equation takes the form

$$\frac{\partial \varphi(x, p)}{\partial x}=-\varphi(x, p) \int_0^{\infty} w(E)\left(1-\mathrm{e}^{-p E}\right) \mathrm{d} E, \tag{21}$$

which can be integrated

$$\varphi(x, p)=\exp \left[-x \int_0^{\infty} w(E)\left(1-\mathrm{e}^{-p E}\right) \mathrm{d} E\right] . \tag{22}$$

From this formula we see that a splitting of the cross section in a sum leads to a product of Laplace transformed distribution functions. The final distribution function will thus consist of a convolution of the distribution functions pertaining to the different parts of the cross section.

Landau solved the kinetic equation for the Coulomb cross section

$$w(E)=\frac{\xi}{x} \frac{1}{E^2} \tag{23}$$

(strictly speaking, eq. (23) is the Thomson formula for Rutherford scattering in a Coulomb field). However, the average energy loss diverges for this cross section, and a non-zero minimum energy transfer ε' is introduced, so that the average energy loss for the Landau distribution equals the Bethe value. The Landau result is the universal function

$$f_{\mathrm{L}}(x, \Delta)=\frac{1}{\xi} \frac{1}{2 \pi i} \int_{\sigma-i \infty}^{\sigma+i \infty} \exp [u \ln u+\lambda u] \mathrm{d} u, \tag{24}$$

with the parameter λ given as

$$\lambda=\frac{1}{\xi}\left[\Delta-\xi\left(\ln \left(\xi / \varepsilon'\right)+1-C\right)\right], \tag{25}$$

where $C = 0.577$ is Euler's constant. The minimum energy transfer is given by

$$\ln \varepsilon' = \ln\left(I^2/2mc^2\beta^2\gamma^2\right) + \beta^2, \tag{26}$$

ignoring the density effect. This gives an unphysically low value for ε' (e.g. for Si: $\varepsilon' \sim 0.05$ eV for $\beta\gamma = 1$); however, for $E_K \ll \xi \ll E_{\max}$ the Landau function is a good approximation to the actual distribution. The minimum energy transfer merely determines the position along the energy axis of the Landau function and has no effect on the shape of the distribution function.

Although $\kappa \ll 1$ for the projectile-target combinations investigated experimentally in the present work, the second condition for the validity of the Landau approach, $\xi \gg E_K$ is not fulfilled in our case. For Si, $E_K \sim 2$ keV and $\xi = 17.81$ [keV/mm] x/β^2, which means that $x/\beta^2 \gg 0.1$ mm.

Since the appearance of the Landau result, different authors [7–9] have tried to take the binding effects into account by expansion of the e^{-pE} term in eq. (22). The distribution function can then be written as the Landau function convoluted with functions, depending on the higher moments of the energy loss of the difference between the actual and the Coulomb cross section. However, these authors only retained the first non-trivial term, corresponding to the second moment of the energy loss which is only a slight improvement to the Landau approach [10], due to the poor convergence of the expansion. This distribution function, which is the Landau function convoluted with a gaussian, has been much used in the interpretation of experiments (for Si, see ref. [11]), letting the width of the gaussian, which actually is given by the second moment of the energy loss, be a free parameter.

Finally, before turning to the model used in comparisons with experimental data in this work, other approaches should be mentioned. Allison and Cobb [3] also started from eq. (2), but a dielectric function extracted from photoabsorption data was used. This approach is, however, only applicable for dilute matter. A Monte Carlo technique was used in refs. [12] and [13] taking into account binding effects. A convolution technique developed by Bichsel [14] has recently been used in comparison with uncalibrated energy-loss data for 5 GeV/c pions passing through a ~ 20 μm thick Si detector [15]. Recently, Lindhard [16] presented an approximation procedure for finding the distribution function. This procedure also allows inclusion of binding effects.

2.3. THE CROSS SECTION MODEL

We shall now describe the model used in comparison with the obtained experimental results. Talman [17] used a similar approach to obtain an analytical expression for the distribution function, although without density effect. We start from eq. (9) by interpreting $\hbar\omega$ as the energy transfer in a collision between the

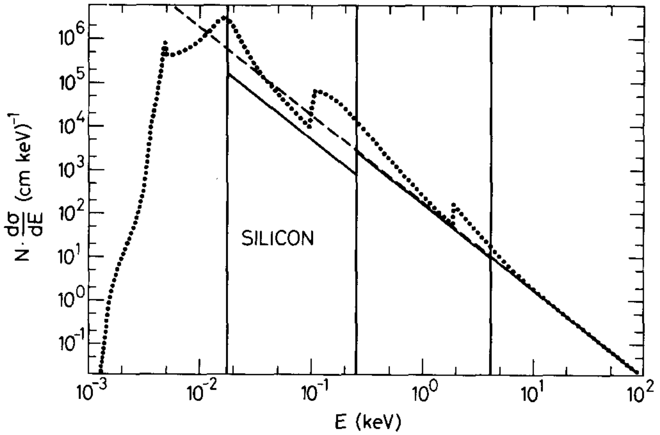

Fig. 1. Collision cross section as function of energy transfer for our model (full-drawn), the Rutherford cross section (dashed) and the cross section from ref. [9] (dotted).

incident particle and the target atoms. We thus get the collision probability as

$$w(E)=\frac{1}{x}\sum_n \xi_n \frac{1}{E_{0n}}\delta(E-E_{0n})\left[\ln\frac{2mc^2\beta^2\gamma^2E_{0n}}{E_{0n}^2+\hbar^2l^2}+\frac{l^2}{\gamma^2\omega_{\rm p}^2}-\beta^2\right]$$

$$+\frac{1}{x}\sum_n \xi_n H(E-E_{0n})/E^2, \tag{27}$$

with $\xi_n=F_n\xi$ and l given by eq. (12). $H(\ )$ denotes the Heaviside function. The δ-function term describes resonance excitations whereas the truncated $1/E^2$ term is due to Coulomb excitations. This cross section is compared to the Rutherford cross section and the cross section by Hall [9] obtained from photoabsorption data, in fig. 1. The model cross section evidently avoids the unphysical minimum energy transfer used in the Landau theory, and also binding effects, clearly reflected in the cross section by Hall are to some extent taken into account.

By introducing the average numbers of resonance collisions $m_{\rm r}$ and Coulomb-type collisions $m_{\rm C}$ for each shell, eq. (27) gives

$$m_{{\rm r}n}=\frac{\xi_n}{E_{0n}}\left(\ln\frac{2mc^2\beta^2\gamma^2E_{0n}}{E_{0n}^2+\hbar^2l^2}+\frac{l^2}{\gamma^2\omega_{\rm p}^2}-\beta^2\right), \tag{28}$$

$$m_{{\rm C}n}=\frac{\xi_n}{E_{0n}}. \tag{29}$$

TABLE 1

In the table is given the number of resonance collisions ($m_{\mathrm{r}n}$), the number of Coulomb-type collisions ($m_{\mathrm{C}n}$), the effective binding energy (E_{0n}), the oscillator strength (F_n) and the corresponding value for $\xi = F_n \xi_n$ for the K, L and the M-shell in 0.1 mm Si

n	K	L	M
$m_{\mathrm{r}n}$	1.04	57.7	330
$m_{\mathrm{C}n}$	0.063	4.22	29.9
E_{0n} (eV)	4033	241	17
F_n	$\frac{2}{14}$	$\frac{8}{14}$	$\frac{4}{14}$
ξ_n (keV)	0.254	1.02	0.509

TABLE 2

As table 1, but for the K, L, M and N-shell in 0.4 mm Ge

n	K	L	M	N
$m_{\mathrm{r}n}$	0.806	24.3	481	1011
$m_{\mathrm{C}n}$	0.050	1.75	41.8	111.8
E_{0n} (ev)	17920	2056	194	16.1
F_n	$\frac{2}{32}$	$\frac{8}{32}$	$\frac{18}{32}$	$\frac{4}{32}$
ξ_n (keV)	0.900	3.60	8.10	1.80

For $\beta\gamma \gg \omega_n/\omega_{\mathrm{p}}$, $l^2 = \beta^2\gamma^2\omega_{\mathrm{p}}^2$, and

$$m_{\mathrm{r}n} = \frac{\xi_n}{E_{0n}} \ln \frac{2mc^2 E_{0n}}{\hbar^2 \omega_p^2}, \qquad \beta\gamma \gg \omega_n/\omega_{\mathrm{p}}. \tag{30}$$

In tables 1 and 2 are given $m_{\mathrm{r}n}$ and $m_{\mathrm{C}n}$ for 0.1 mm Si and 0.4 mm Ge, respectively, for $\beta\gamma \gg \omega_n/\omega_{\mathrm{p}}$. It is to be noted, that m_{r} is around a factor of 10 larger than m_{C}. With the above definition of $m_{\mathrm{r}n}$ and $m_{\mathrm{C}n}$ the collision probability is given by

$$w(E) = \frac{1}{x}\left[\sum_n m_{\mathrm{r}n}\delta(E - E_{0n}) + m_{\mathrm{C}n}E_{0n}H(E - E_{0n})/E^2\right]. \tag{31}$$

Talman [17] showed by using Laplace transforms, that the distribution function corresponding to the above cross section can be given analytically, but the evaluation of his expression is difficult when x is small.

Now the cross section is split into the resonant and the Coulomb-part, and then again into one part for shells with few collisions and a part for shells with many collisions.

With the cross section from eq. (31) the Laplace-transformed distribution function is given by

$$\varphi(x, p) = \exp\left[-m_{\mathrm{r}}(1 - \mathrm{e}^{-pE_0})\right] \exp\left[-m_{\mathrm{C}} E_0 \int_{E_0}^{\infty} \frac{1 - \mathrm{e}^{-pE}}{E^2}\, \mathrm{d}E\right]. \tag{32}$$

The shell-index n has here been omitted. Expanding the exponential in the exponent, for the resonance excitations we get:

$$\varphi_{\mathrm{r}}(x, \Delta) = \mathrm{e}^{-m_{\mathrm{r}}} \sum_{k=0}^{\infty} \mathrm{e}^{-pkE_0} m_{\mathrm{r}}^k / k!. \tag{33}$$

Performing the inverse Laplace transformation, the distribution function for the resonance collisions is given by

$$f_{\mathrm{r}}(x, \Delta) = \sum_{k=0}^{\infty} \frac{\mathrm{e}^{-m_{\mathrm{r}}} m_{\mathrm{r}}^k}{k!} \delta(\Delta - kE_0), \tag{34}$$

which is nothing other than the Poisson distribution function. When $m_{\mathrm{r}} \ll 1$, $f(x, \Delta) \approx \delta(\Delta)$, so that the shells with $m_{\mathrm{r}} \ll 1$ practically do not participate in the formation of the distribution function through their resonance collisions. For the Coulomb-type collisions we have

$$\varphi_{\mathrm{C}}(x, p) = \exp\left(-m_{\mathrm{C}} E_0 \int_{E_0}^{\infty} \frac{1 - \mathrm{e}^{pE}}{E^2}\, \mathrm{d}E\right) \tag{35}$$

and

$$f_{\mathrm{C}}(x, \Delta) = \frac{1}{2\pi i} \int_{-i\infty+\sigma}^{+i\infty+\sigma} \exp\left(p\Delta + m_{\mathrm{C}} E_0 \int_{E_0}^{\infty} (\mathrm{e}^{pE} - 1) E^{-2}\, \mathrm{d}E\right) \mathrm{d}p, \tag{36}$$

which, introducing $t = pE_0$ gives

$$f_{\mathrm{C}}(x, \Delta) = \frac{1}{E_0} \frac{1}{2\pi i} \int_{-i\infty+\sigma}^{+i\infty+\sigma} \exp\left(m_{\mathrm{C}}\left[\frac{\Delta t}{E_0 m_{\mathrm{C}}} - 1 + E_2(t)\right]\right) \mathrm{d}t, \tag{37}$$

where $E_2(t)$ is the exponential integral. When $m_{\mathrm{C}} \ll 1$:

$$f_{\mathrm{C}}(x, \Delta) = \mathrm{e}^{-m_{\mathrm{C}}}\left[\delta(\Delta) + \frac{m_{\mathrm{C}} E_0 H(\Delta - E_0)}{\Delta^2}\right]. \tag{38}$$

For a large number of Coulomb-type collisions, $m_{\mathrm{C}} \gg 1$, the distribution function for these collisions, not surprisingly, is given by the Landau function (24) with $\lambda = \Delta/\xi - (\ln(\xi/E_0) + 1 - C)$. For arbitrary m_C the following approximation will be used

$$f_C(x, \Delta) = e^{-m_C}\delta(\Delta) + (1 - e^{-m_C})\left[\frac{E_0}{\Delta^2}\int_0^{E_0} f_L(x, \Delta')\,d\Delta' + f_L(x, \Delta)\right] H(\Delta - E_0). \tag{39}$$

It is seen that this expression is correct in the limits $m_C \ll 1$ and $m_C \gg 1$, and that it is normalized. Also for intermediate values of m_C, eq. (39) is a good approximation to eq. (37).

To summarize: The distribution function for the Coulomb-type collisions from the shells with $m_C \geq 10$ is a Landau function with parameters given as

$$\xi = \sum_{\substack{n \\ m_{Cn} \geq 10}} \xi_n, \qquad \lambda = \frac{\Delta}{\xi} - \left(\ln\frac{\xi}{I} + 1 - C\right), \qquad \ln I = \sum_{\substack{n \\ m_{Cn} \geq 10}} F_n \ln E_{0n}. \tag{40}$$

For shells with $m_r \geq 10$, the Poisson distribution, eq. (34), is replaced by a gaussian,

$$f_r(x, \Delta) = \frac{1}{\sqrt{2\pi}\,\sigma_r} e^{-(\Delta - \bar{\Delta}_r)^2/2\sigma_r^2}, \tag{41}$$

where $\bar{\Delta}_r = m_r E_0$ and $\sigma_r = \sqrt{m_r}\,E_0$. Thus the distribution function for the resonance collisions from shells with $m_r \geq 10$ is given by (41), with

$$\bar{\Delta}_r = \sum_{\substack{n \\ m_{rn} \geq 10}} m_{rn} E_{0n}, \qquad \sigma_r^2 = \sum_{\substack{n \\ m_{rn} > 10}} m_{rn} E_{0n}^2. \tag{42}$$

For shells with m_r or $m_C < 10$ the distribution function has been calculated from (34) or (39) directly. Finally the resonance and the Coulomb-type contributions are convoluted, to give the final distribution function.

2.4. MODEL CALCULATIONS

We shall now, before showing calculated distributions, discuss qualitatively the results of the above model. The width of the Landau distribution is independent of the binding energies, E_{0n}, being given simply as 4.02ξ. In the same way, the Coulomb contribution to the width from shells with many Coulomb-type collisions is independent of the binding energies of the electrons and proportional to their number. When m_C is small a width cannot be ascribed to the distributution function for the Coulomb collisions. For the resonance collisions, the width of the

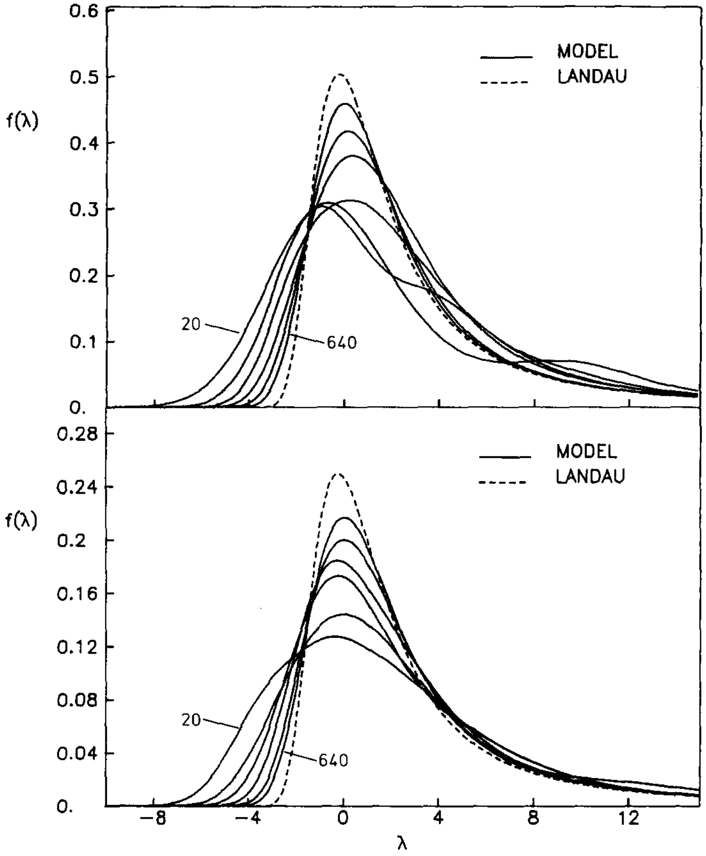

Fig. 2. Distribution functions for 2 GeV/c pions traversing 20, 40, 80, 160, 320 and 640 μm Si (upper part) and Ge (lower part). The Landau function is shown for comparison. The distribution functions are shown as function of the Landau parameter λ.

distribution is proportional to the binding energy, $\sigma_r = \sqrt{m_r} E_0$, when $m_r > 1$. For $m_r \lesssim 1$, the resonance collisions lead to a redistribution in the energy-loss function. Since $\sigma_r \propto \sqrt{x}$ and $\xi \propto x$, it is the resonance collisions from inner shells which, in spite of their small number, for thin targets lead to broadening of the distribution function, as compared to the Landau distribution.

The Landau function and the distribution function from the above model for 2 GeV/c pions from the above model traversing 20, 40, 80, 160, 320 and 640 μm Si and Ge are shown in fig. 2. The choice of the used excitation energies will be discussed later. It is seen that the present model converges towards the Landau function for large thicknesses. The distribution broadens for decreasing thickness due to the decreasing number of resonance collisions. When $m_{rK} \sim 1$, shoulders appear on the high-energy side of the distribution, corresponding to 1, 2,... K-shell

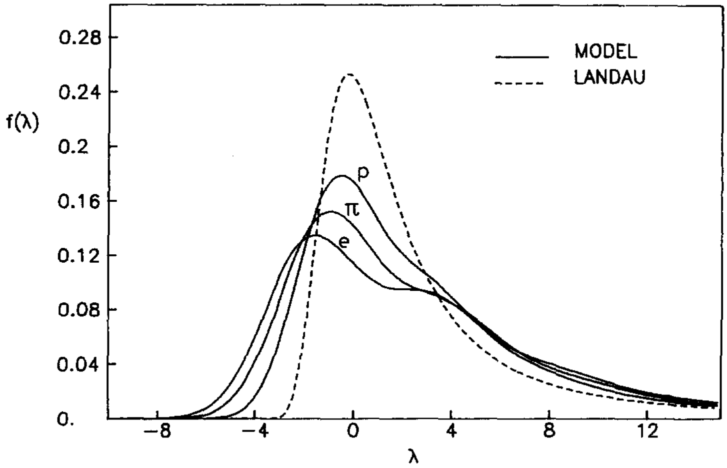

Fig. 3. Distribution functions for 2 GeV/c e, π and p penetrating 40 μm Si. The Landau function is shown for comparison. The distribution functions are shown as function of the Landau parameter λ.

excitations. This happens between 40 and 80 μm in Si and between 160 and 320 μm in Ge. At the same time, the most probable energy loss shifts to a lower value, since the K-shell electrons no longer contribute to the most probable energy loss. For $m_{\mathrm{rK}} \ll 1$, the K-shell electrons also do not contribute to the FWHM of the distribution. In the case of Ge, $m_{\mathrm{rL}} \sim 1$ for 20 μm and the Poisson character of the distribution function for the L-shell resonance collisions becomes visible. The shoulder on e.g. the 20 and 40 μm Si spectrum is not to be expected as marked in experimental spectra, since it is a result of the δ-function representation of the atomic binding, cf. fig. 1.

The $\beta\gamma$-dependence of the distribution function is weak for $\beta\gamma > 1$, although the density effect becomes effective at different γ-values for the different shells. The number of resonance collisions saturates at $\beta\gamma \sim E_{0n}/\hbar\omega_{\mathrm{p}}$ (cf. eq. (30), which for Si gives $\beta\gamma \sim 60$, 5 and 1 for the K, L and M-shell, respectively. In fig. 3 is shown the distribution function for 2 GeV/c electrons, pions and protons on 40 μm Si. The increasing number of K-shell resonance excitations with γ is clearly visible.

Finally, in figs. 4 and 5 are shown the most probable energy loss and the width of the distribution for 2 GeV/c pions as function of thickness in the case of Si and Ge. For large thicknesses the most probable energy loss is slightly above the Landau value. At ~ 100 μm Si and $x \sim 300$ μm Ge the most probable energy loss decreases faster with decreasing thickness than the Landau value due to the "switching-off" of the K-shell excitations. For much smaller thicknesses the most probable energy loss is independent of the K-shell excitations. The width of the distributions increase with decreasing target thickness until a maximum is reached at $x \sim 50$ μm Si and $x \sim 150$ μm Ge. For much smaller thicknesses the K-shell electrons no longer

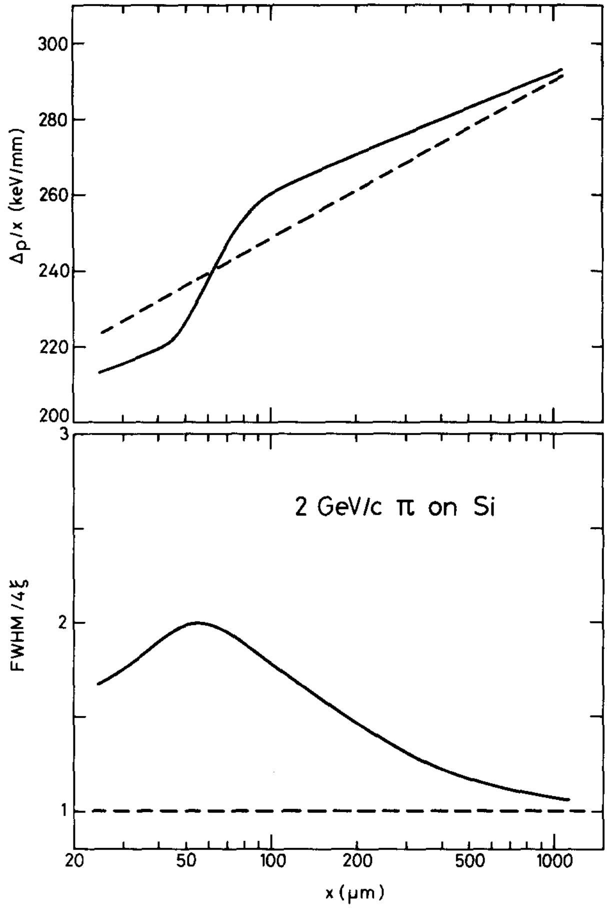

Fig. 4. Most probable energy loss (Δ_p/x) and width (FWHM/ξ) of the energy-loss distribution for 2 GeV/c pions as function of thickness Si. The dashed curve is the Landau result.

contribute to the FWHM of the distribution, and the width increases again now due to the resonance excitations of L-shell electrons.

The excitation energies characterizing the solid are taken from measurements of plasma frequencies and ionization potentials, refs. [18–22]. For the M-shell in Si and the N-shell in Ge, Ω_{0n} is taken as the plasma frequency. The other excitation energies are taken as ionization potentials scaled to give the correct mean ionization potentials [22], $I = 169$ eV in Si and $I = 340$ eV in Ge. In this way, the excitation energies given in tables 1 and 2 are obtained.

2.5. MEAN, RESTRICTED AND MOST PROBABLE ENERGY LOSSES

In subsect. 2.1, the mean, or average, ionization energy loss of relativistic charged particles passing through thin foils was calculated. This average energy loss is what

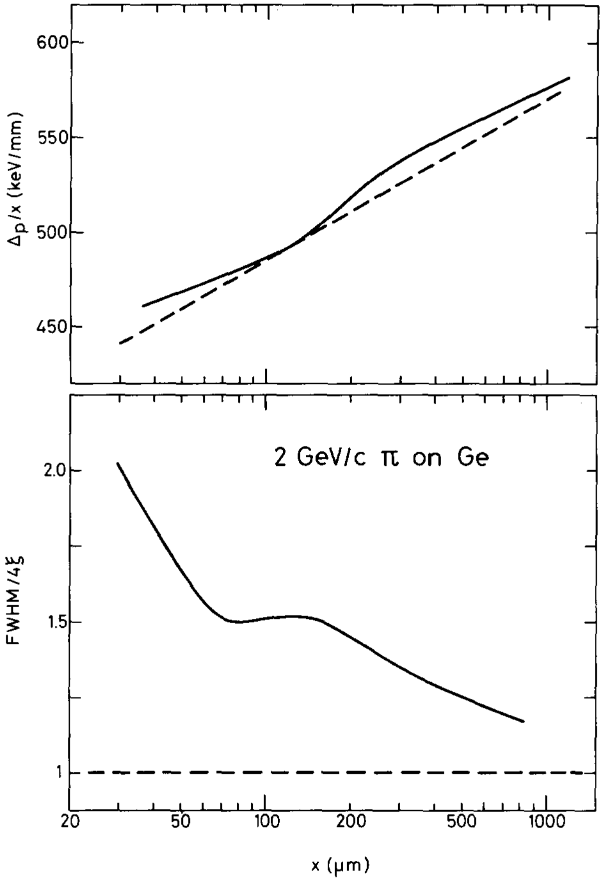

Fig. 5. As fig. 4, but for Ge.

is measured in classical experiments, as the difference in the projectile energy before and after the passage of the foil, averaged over many particles. For high-energy particles, this approach is not feasible, due to the very small energy loss less than 100 keV as compared to projectile energies of several GeV. A different approach is used in this work, namely to measure the energy deposited in the target. This can be done when the target is a fully depleted semiconductor detector. What is now the difference between the measured deposited energy and the calculated average energy loss? Energy escapes the foil (see also subsect. 3.2) mainly as kinetic energy of δ-rays. If the maximum energy transfer $E_{\max}$ in the Bethe formula is replaced by a constant $E_0 < E_{\max}$, we get the formula for the restricted energy loss, restricted in the sense that energy transfers are restricted to $E < E_0$

$$\Delta_{\text{restr}} = \xi \left\{ \ln \frac{2mc^2\beta^2\gamma^2 E_0}{I^2} - \frac{E_0}{2mc^2\gamma^2} - \beta^2 - \delta \right\}. \tag{43}$$

The energy loss, to be compared to measured deposited average energy losses, should then be the above restricted energy loss, E_0 being given as the kinetic energy of an electron of range of the order of the target thickness [23]. For 1 mm Si, we get $E_0 \sim 500$ keV. The exact choice of E_0 is not very important, due to the weak dependence of the above formula on E_0. Also this restricted energy loss is not easily comparable to measurements, due to the high-energy tail in the energy-loss distribution. An experimentally well defined quantity is the most probable energy loss. To calculate the most probable energy loss in principle it is necessary to know the energy-loss distribution function. For the Landau function, the maximum occurs at [24]

$$\lambda = -0.225, \qquad \lambda = \left[\Delta - \xi\left(\ln\frac{2mc^2\beta^2\gamma^2\xi}{I^2} + 1 - C - \beta^2 - \delta\right)\right]\Big/\xi, \tag{44}$$

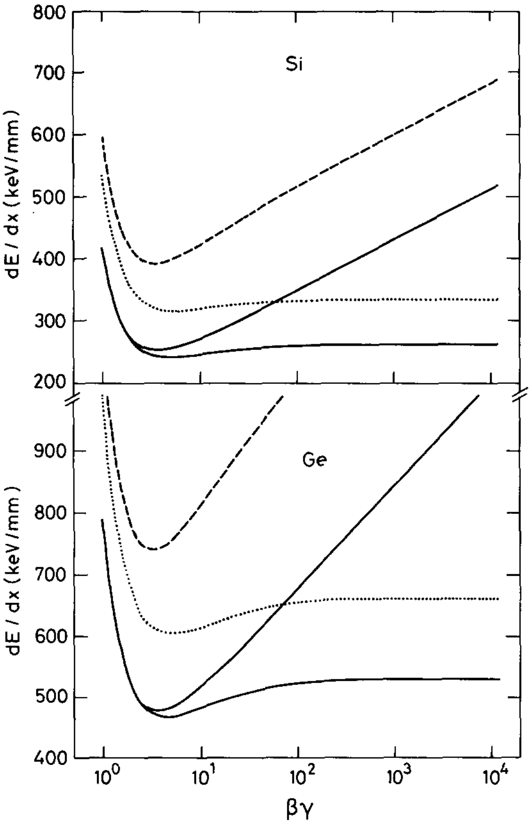

Fig. 6. Most probable (full-drawn), restricted (dotted) and average (dashed) energy loss in Si and Ge as function of $\beta\gamma$. For details, see the text.

giving for the most probable energy loss

$$\Delta_{\mathrm{p}} = \xi\left[\ln\frac{2mc^2\beta^2\gamma^2\xi}{I^2} + 0.198 - \beta^2 - \delta\right]. \tag{45}$$

In fig. 6 is shown the most probable energy loss, eq. (45), with (lower full-drawn curve) and without (upper full-drawn curve) density effect. Also shown is the restricted energy loss, eq. (43), dotted and the average energy loss, eq. (10), dashed, both including density effect. The curves have been calculated for 0.1 mm Si and 0.4 mm Ge.

Escape of δ-rays will also lead to changes in the energy-loss distribution, mainly at $\Delta \gg E_0$. However, the probability of producing a δ-ray with sufficient energy to escape the detector is at the one percent level, decreasing for decreasing target thickness and the δ-rays is not expected to give any appreciable broadening [9].

3. Experimental considerations

3.1. GENERAL LAYOUT

The experiment was performed at the beam-line t7 at the CERN Proton Synchrotron. Secondary particles, mostly e^+/e^-, π^+/π^-, K^+/K^- and $p/\bar{p}$, produced in the production target can be transported by the beam-line elements at momenta between 0.5 and 10 GeV/c. The divergence of the beam was typically 2 mrad and the beam size 10–20 mm, largest at the small momenta. The intensity could be varied between 10^3 and 10^6 particles per burst (450 ms). The momentum bite used was typically 0.2%.

The last part of the beam line and the experimental area is shown in fig. 7. The useful part of the beam was defined by the scintillators, SC. The anticoincidence counter, $\overline{\mathrm{SC}}$, vetoed particles hitting the target at distances larger than 6 mm from the center. The position of the particles was registered by the drift chambers, DC1-DC2-DC3, to an accuracy of ~ 0.1 mm. The particle-type was identified with the Čerenkov counters, C1 and C2, and the lead glass array, LG. A vacuum system

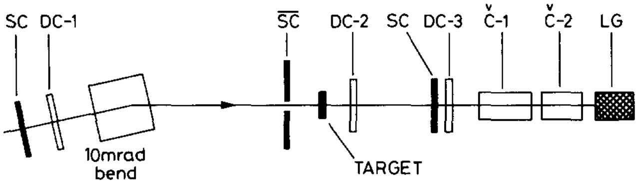

Fig. 7. Schematic drawing of the experimental setup. DC designates drift chamber, SC: scintillator, C: Čerenkov counter and LG: lead-glass array.

(pressure $< 10^{-5}$ torr) surrounded the beam from DC1 throughout DC2. The beam was cleaned by the 10 mrad dipole magnet, so that radiation, mainly photons, created upstream, did not hit the target.

Due to the very small content of kaons (less than 1%), it was decided only to use three kinds of particles, namely protons, pions, and electrons. This decision was also made in view of the limited space in the beam line. Two Čerenkov counters were used, one tuned for electron/muon separation and one for pion/kaon separation. In this way, the ~ 1% muons from pion decay were included with the 30–50% pions and the ~ 1% kaons with the 10–50% protons. In this way, the errors introduced by the muon and the kaon content of the beam, was less than other, mainly statistical, uncertainties, due to the relatively slow variation of the energy loss with γ. At 2 GeV/c, the protons were identified by time-of-flight. The electrons were also identified with the lead-glass array.

The data acquisition was done in the following way. The trigger logics selected the interesting events to be transferred to tape. The interesting events are events in the useful part of the beam, defined by the scintillation counters, giving a signal in the semiconductor target and which is well separated from the previous and the next particle in the burst. It was further required that the data taking system (computer and CAMAC system) was idle.

The particle identification was done in the hardware, apart from the electron identification by the lead glass. So the particle identification data consisted of the particle identification bit-pattern plus the lead glass ADC signals. Furthermore, the events consisted of TDC data from the drift chambers and ADC data from the energy-loss detector. The arrival of the energy-loss signal relative to the beam particle was also recorded in a TDC. Various other signals were also recorded, either for each event or each burst, to check the correct performance of the experiment. A minicomputer, used to transfer events to tape, was also used for monitoring the experiment. Beam profiles, energy-loss spectra, lead-glass spectra, etc. could be displayed on this minicomputer.

The drift chambers were mainly used to exclude particles hitting the edge of the active area of the energy-loss detectors. These particles give a reduced energy-loss signal since they penetrate partially depleted regions of the detector, and they appear in the energy-loss spectra mainly as a low-energy tail. However, a fraction of this tail remains, after reducing the beam size with the drift chambers, probably due to inefficiencies in the drift chambers (see also sect. 4). The low-energy tail is removed in the comparison with calculations to improve the normalization.

3.2. ENERGY LOSS DETECTION

The Si detectors used in the experiment were commercial EG&G ORTEC totally depleted surface barrier detectors. Their dimensions are given in table 3. These detectors have a maximum thickness variation of ± 0.5 μm and ± 1.0 μm for the

TABLE 3
Thickness (x), active area (A) and resolution (σ) of the Si detectors used

x (μm)	32.0	50.9	100.3	174.0	290	1040
A (mm^2)	10	10	50	50	50	50
σ (keV)	0.784	0.730	2.00	3.51	3.18	3.95

three thin and the three thick detectors, respectively. This thickness uniformity assures that no additional broadening of the energy-loss distribution is caused by thickness variations. We also present results from measurements using a 0.370 mm Ge detector. This detector was fabricated as described in ref. [23].

As we were interested in the width of the energy-loss distribution, it was necessary to operate the detector and the amplifier system in such a way, that the noise was much smaller than the width of the energy-loss distribution. It was thus necessary to cool the 3 thin detectors, to eliminate the noise contribution from leakage current. Furthermore the 2 thin detectors had a very small active area, to reduce the noise caused by detector capacitance. In this way resolutions (RMS value of gaussian) as given in table 3 were achieved. For the Ge detector a resolution of $\sigma = 3.5$ keV was obtained. Finally it should be mentioned that pile-up did not lead to any observable deteoriation of the energy-loss spectra.

The detectors were calibrated using a Ba-133 source emitting X- and γ-rays, and a precision pulser. The detectors were calibrated before and after each run, and no detectable drift in the calibration constants, nor in the resolution, was found.

Calibrating detectors, used to measure energy loss of GeV particles, with γ-rays, assumes that the energy required to produce an electron/hole pair, w, is the same for the two processes. This is a reasonable assumption as differences from w for fast electrons, protons and photons have only been found for low-energy α-particles and heavy nuclei [25]. Furthermore, the production of electron/hole pairs leads to additional broadening. An intrinsic resolution, with variance $\sigma^2 = F\Delta E w$, exists due to the electron/hole pair statistics [26]. Here ΔE is the energy lost by the projectile and $F \sim 0.10$, the Fano factor, accounts for the fact, that the formation of the different electron-hole pairs are strongly correlated. This intrinsic resolution is, even for our thinnest detector, much smaller than the electronical noise, and can thus be neglected.

We shall also briefly discuss processes, different from the primary ionization energy-loss process, in which energy may enter or escape the target, thus making difficult comparisons between measured deposited energies and calculated ionization energy losses. A detailed evaluation of these processes has been made in ref. [27]. There is a large difference between the average energy loss and the average deposited energy loss due to escape of δ-rays. However, the most probable energy loss is uninfluenced by these high-energy δ-rays (see subsect. 2.5). Energy may also escape the detector in the form of X-rays, photoelectrons, and Čerenkov radiation, and energy from transition radiation and bremsstrahlung may be absorbed.

When K-shell vacancies are created, the emitted electron or the subsequently emitted X-ray of Auger electron may escape the detector. Because of the very small fluorescence yield and because of the short range of low-energy electrons these escapes have very little influence on the spectra.

Čerenkov radiation emitted in regions of low absorption may also escape the detector. Čerenkov radiation is, however, mainly emitted at low frequencies, where the absorption is large, and the non-absorbed radiation is negligible. It should be mentioned here, that the energy loss due to Čerenkov radiation is included in the calculation presented in sect. 2.

Transition radiation and bremsstrahlung, only emitted in substantial amounts in the target by electrons, may be absorbed in the target. Only the energetic part of the photons can influence the measurements, and for these photons the absorption length is much larger than the target thicknesses.

In conclusion, what is measured as the number of liberated carriers in the target are closely proportional to the ionization energy loss, for not too large energy losses.

4. Discussion of results

4.1. ENERGY LOSS AND STRAGGLING IN Si

Energy-loss distributions have been obtained for 2 GeV/c p, π^+ and e^+ on 32.0, 50.9, 100.3, 174, 290 and 1040 μm Si and for 8 GeV/c p, π^+ and e^+ on 174, 290 and 1040 μm Si. In the negative polarity, energy-loss distributions have been recorded for 2 and 8 GeV/c for the 290 and the 1040 μm Si detector. We only show the energy-loss distributions for 2 GeV/c positive particles on the 6 Si targets in figs. 8–13. Also shown is the Landau distribution function (dashed) and the distribution function obtained from the model described in subsect. 2.3 (full-drawn). The Landau function is shown as a reference, to see the importance of electronic binding effects. The theoretical distribution functions have been convoluted with the resolution function, a gaussian with a width given by the resolutions quoted in table 3. Although the width of the resolution function is smaller than the width of the distribution function, it leads to some broadening, especially for the 32.0 μm detector.

The general observation is that the measured distributions follow nicely the broadening of the model distribution function, as compared to the Landau function, for decreasing thickness. Also the downward shift of the most probable energy loss, again as compared to the Landau function, seems to be reproduced.

To study quantitatively the agreement between measured widths and most probable energy losses and model predictions, in figs. 14–19 we have plotted, measured and calculated (including resolution) values for the most probable energy

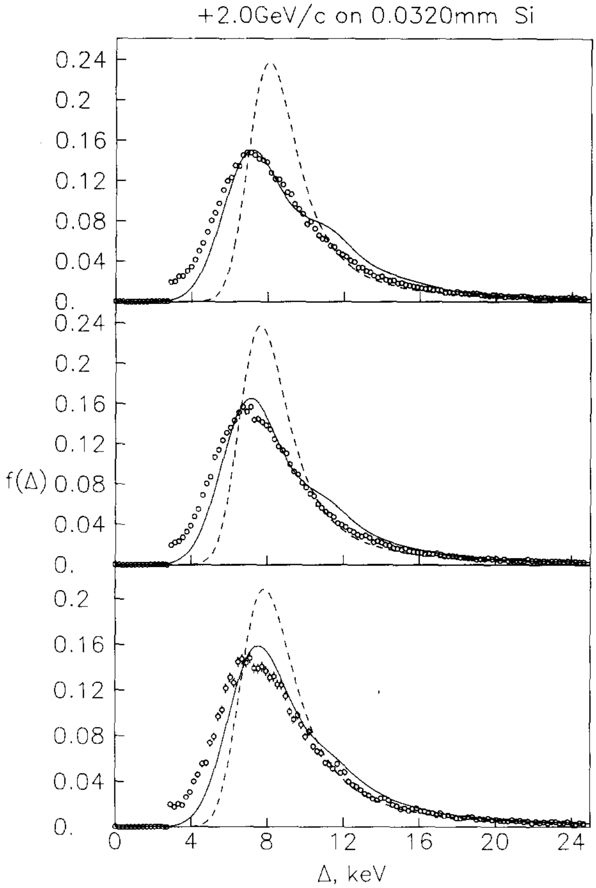

Fig. 8. Experimental energy-loss distributions compared to the Landau function (dashed) and the distribution function from our model (full-drawn). The upper spectrum is for 2 GeV/*c* positrons, the middle for 2 GeV/*c* pions and the lower for 2 GeV/*c* protons traversing the 32.0 μm Si target.

loss (in keV/mm) and for the width (FWHM/ξ), as function of $\beta\gamma$ for the 6 different thicknesses. The measured values have been extracted by fitting a polynomial of order 8 to the data. Only data points with a content of more than ~ 25% of the maximum content are used in the fit. Increasing the order of the polynomial does not change significantly the extracted values.

Although the results from the model were discussed in subsect. 2.3, we shall here briefly comment on the theoretical curves on figs. 14–19.

The most probable energy loss from the model is below the Landau value for the two thin detectors and above for the other, due to the separation of collisions with one or more K-shell excitations from collisions with none for the thin targets. Both the Landau and the model most probable energy loss are proportional to β^{-2} for

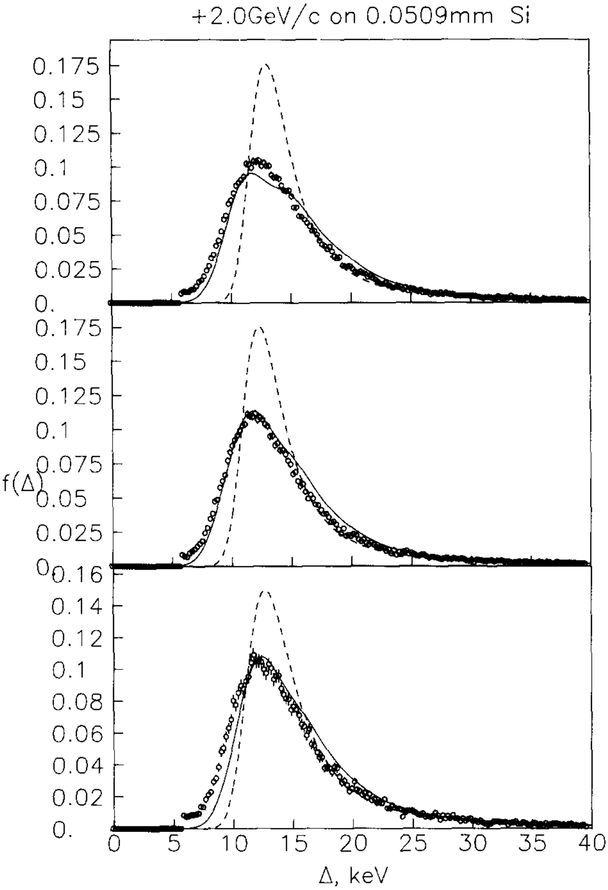

Fig. 9. As fig. 8 but for the 50.9 μm Si target.

$\beta\gamma \lesssim 1$, has a minimum for $\beta\gamma \sim 4$ and saturate at the Fermi plateau for $\beta\gamma \gtrsim 50$.

The FWHM of the Landau distribution is 4.02ξ, and the amount, that the width of the Landau distribution convoluted with the resolution function is above 4.02ξ, reflects the broadening due to the finite resolution. The decrease for $\beta\gamma \lesssim 2$ in FWHM/ξ for the Landau distribution including resolution is caused by the β^{-2} increase in the energy loss for decreasing β.

The width of the model distribution is larger than the Landau function, up to almost a factor of two for the 32.0 μm detector. For the two thin detectors the FWHM/ξ does not saturate until $\beta\gamma \sim 100$, due to the saturation of the K-shell excitations at this value of $\beta\gamma$. For the thicker detectors, this saturation takes place at smaller $\beta\gamma$-values due to the smaller contribution of the K-shell excitations to the width of the distribution for large thicknesses.

We shall now discuss figs. 8–19, one thickness at a time.

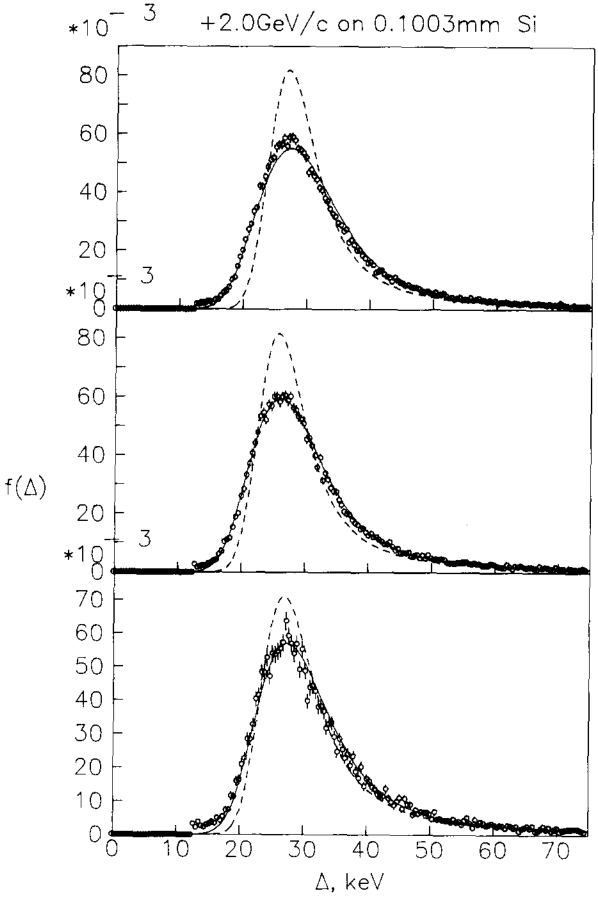

Fig. 10. As fig. 8 but for the 100.3 μm Si target.

32.0 μm. The shoulder on the high energy side of the model distribution is not reproduced in the experiment. This shoulder, involving exactly one K-shell excitation, is caused by the unphysical δ-function representation of the resonance collisions in the collision cross section, cf. fig. 1. It is thus not to be expected as distinct in the experimental spectra. The agreement between the measured and the calculated distribution function is clearly not very good on the low energy side, the experimental one being significantly above the calculated. This may, at least partly, be due to the low energy tail, remaining when the edge of the detector is excluded. The level of this tail at the point of the cut-off, is clearly visible. In conclusion, the measured distributions are clearly 10–15% too wide with a most probable energy loss ~ 4% too high, as compared to the model calculations. The more pronounced shoulder at high γ-values is responsible for the better agreement between the widths for 2 GeV/c e^+.

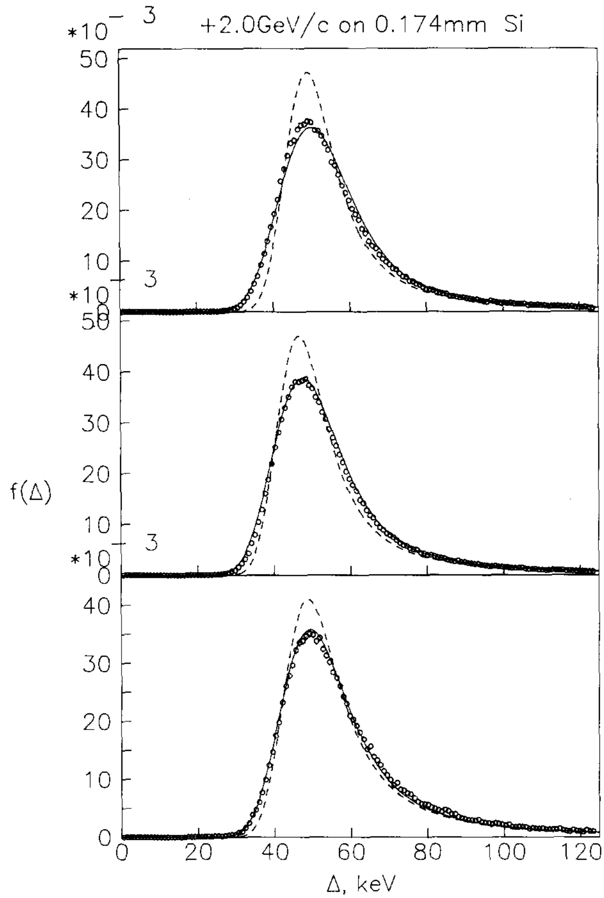

Fig. 11. As fig. 8 but for the 174 μm Si target.

50.9 μm. The one K-shell excitation shoulder is still visible in the model distribution function, although it is closer to the peak. Indications of a weak shoulder in the experimental spectra seem to exist, but the distinct shoulder in the model distribution is not seen, for good reasons as explained above. The width and the most probable energy loss are in reasonable good agreement with calculated values (within a couple of percent), especially considering the distinct shoulder on the model distribution. However, the experimental spectrum is above the theoretical distribution function on the low energy side and below on the high energy side. This is, at least partly, due to the low energy tail on the experimental spectrum and the shoulder on the theoretical distribution function.

100.3 μm. At this thickness the one K-shell excitation shoulder is not visible, since it is very close to the peak of the distribution. The agreement between the

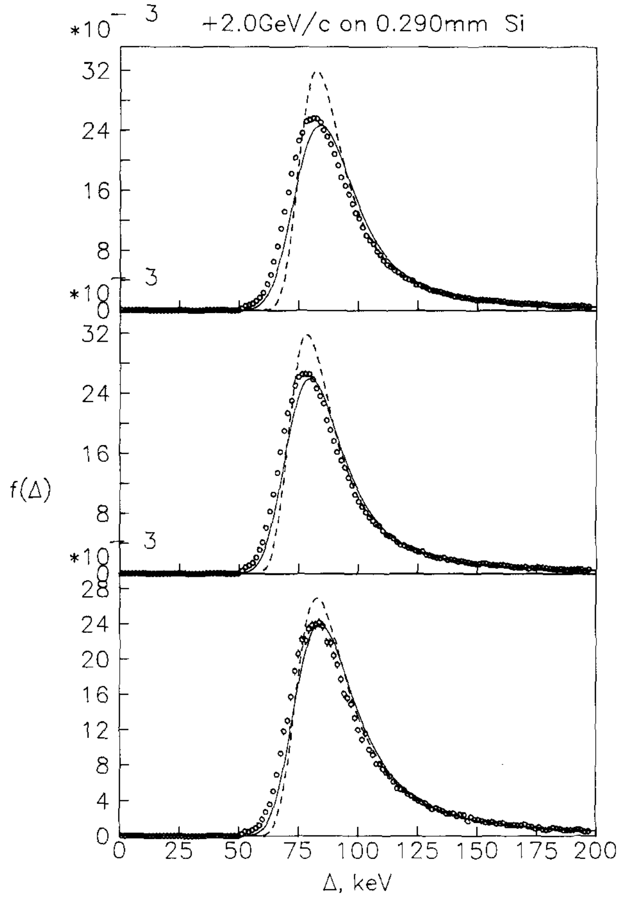

Fig. 12. As fig. 8 but for the 290 μm Si target.

experimental spectrum and the model calculation is almost perfect, but a small discrepancy between the heights of the distributions exists for 2 GeV/c e^+. The low energy tail is very small due to the more favourable ratio between the area and the circumference of the detector, as compared to the two previous cases. The two thin detectors have an active area of 10 mm^2 whereas the present and the three thicker detectors have an area of 50 mm^2. The experimental distributions are 5–7% narrower than the model calculation. The most probable energy loss for 2 GeV/c π^+ and p agrees perfectly with the model calculations but for 2 GeV/c e^+ the experimental value is 3% too low.

174 μm. Very good agreement between experimental spectra and model calculations exist at 2 GeV/c, but for 8 GeV/c pions and protons, the experimental spectra are ~10% narrower than the model result and the experimental most probable energy loss is 3–4% lower than the theoretical value.

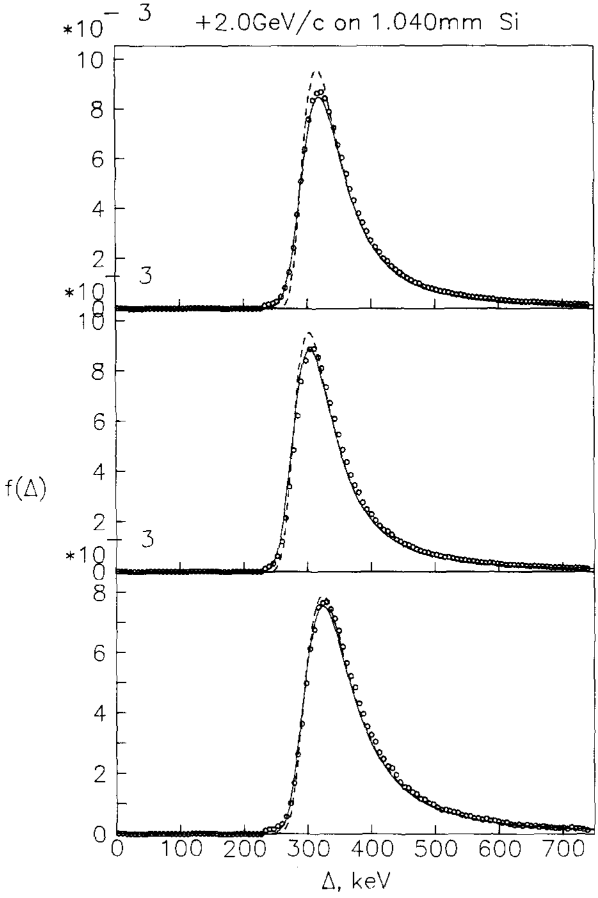

Fig. 13. As fig. 8 but for the 1040 μm Si target.

290 μm. Here all 2 and 8 GeV/c experimental spectra in both polarities are shifted downwards by ~ 4%, but the experimental widths agree well with the widths of the model distribution function. This discrepancy is suspected to be due to a depletion layer ~ 4% thinner than the actual thickness, but it has not been possible to confirm or disprove this suspicion. Finally, notice the very good agreement between width and most probable energy loss for particles of positive and negative charge to better than one percent.

1040 μm. The agreement between experimental spectra and the model calculations is very good, and the small difference between the model distribution function and the Landau function, most clearly visible in the height of the distributions, is well-produced, in the sense that the experimental spectra agree much better with the model distribution function than with the Landau function. Again results for positive and negative particles agree perfectly.

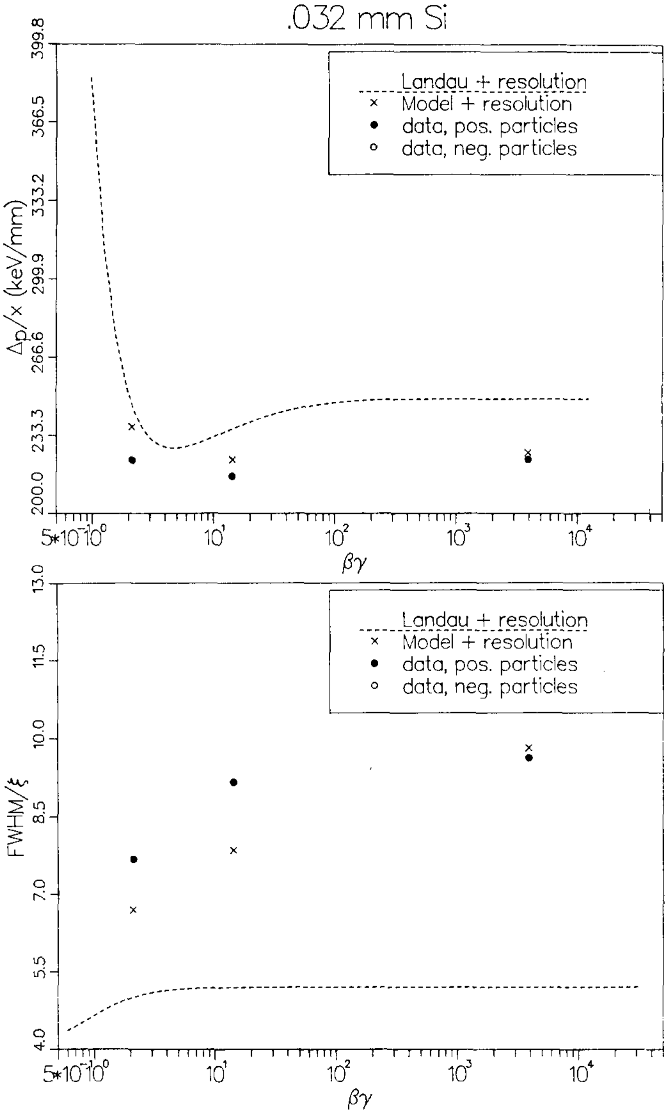

Fig. 14. Most probable energy loss, Δ_p, divided with thickness, x, and width, FWHM, divided with the Landau parameter, ξ, as function of $\beta\gamma$ for the 32.0 μm Si target.

Let us finally make a comment on other measurements known to the authors. A few scattered results exist on the energy-loss distribution for relativistic particles in solid, particularly silicon, targets. Except for the results in ref. [28], they are all for thicknesses larger than 200 μm [11,23,29–32] and none of these measurements are absolute. Either no energy calibration (e.g. with a γ-source) has been performed, or the thickness of the active layer is unknown. These results are thus of limited value, and they are not easily combined to show systematic trends.

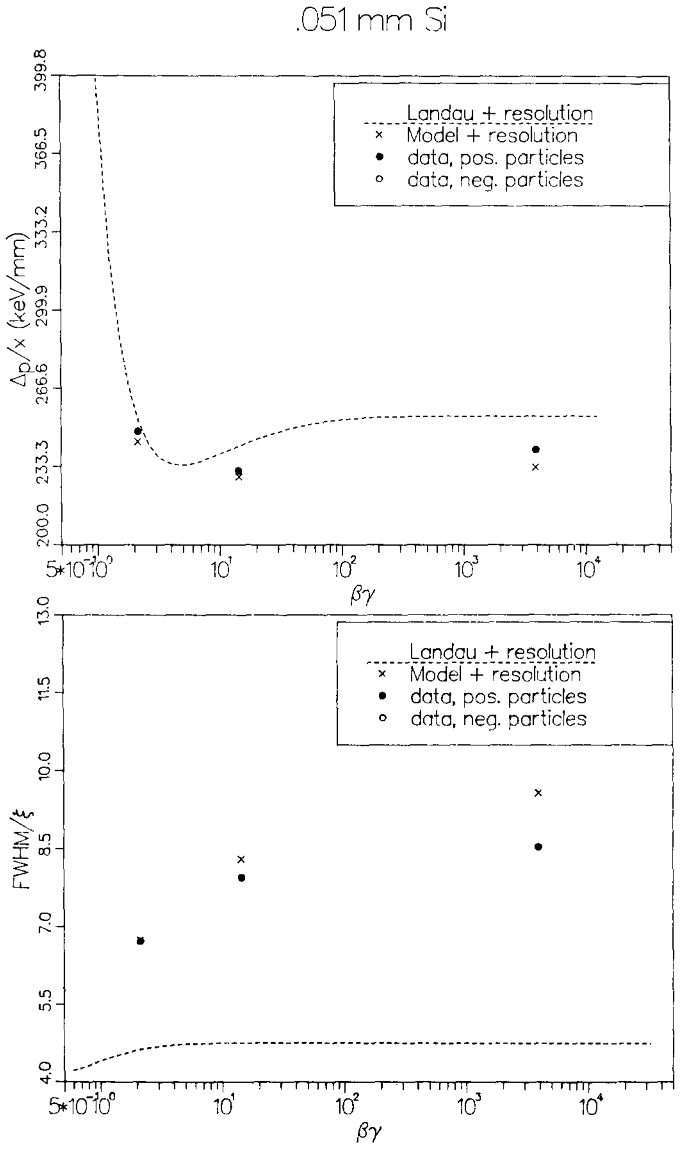

Fig. 15. As fig. 14, but for the 50.9 μm Si target.

4.2. ENERGY LOSS AND STRAGGLING IN Ge

The only data to be discussed for Ge is the energy loss of 8 GeV/c positrons, pions, and protons in a 370 μm Ge detector. This is mainly due to the difficult operation and fabrication of Ge detectors.

The experimental energy loss distributions for 8 GeV/c e^+, π^+, and p are in fig. 20 compared to the Landau distribution (dashed) and the distribution function

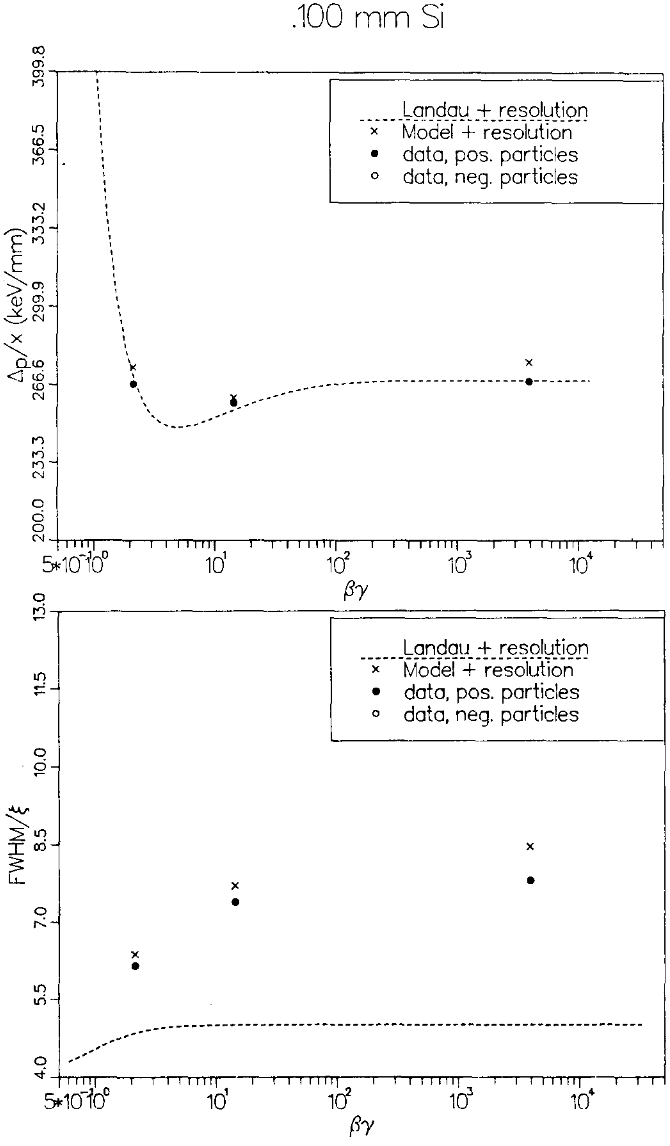

Fig. 16. As fig. 14, but for the 100.3 μm Si target.

calculated from the model described in subsect. 2.3. The experimental resolution is a negligible effect. Very good agreement exists between experiment and the model, both for the most probable energy loss and the width of the distribution as for the distribution function itself. So the additional broadening of the distribution mainly due to the non-negligible binding energy of the K-shell electrons in Ge is well reproduced in the experiment.

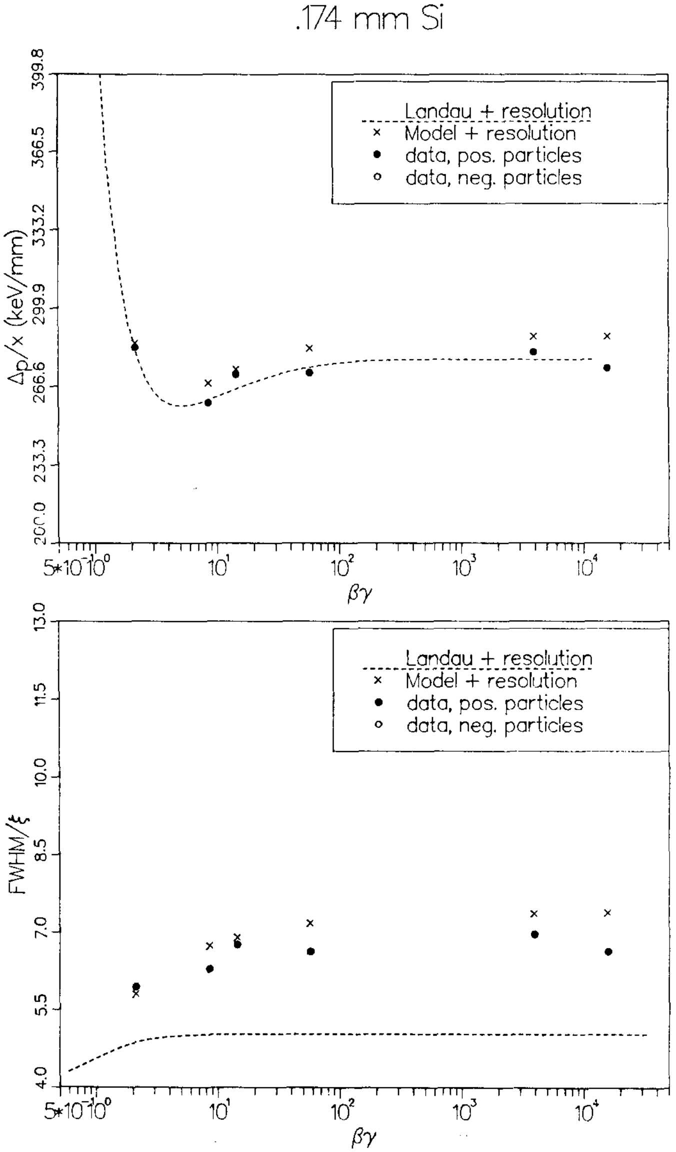

Fig. 17. As fig. 14, but for the 174 μm Si target.

4.3. ULTRA-RELATIVISTIC EFFECTS IN ENERGY LOSS

The Bethe-Bloch formula as described in sect. 2 needs modifications at ultra-relativistic velocities, i.e. for $\gamma \gg 1$, such as radiative corrections, kinematic corrections, projectile-structure corrections etc. These corrections, however, seem to apply only to the average energy loss, and not to have any influence on restricted and most

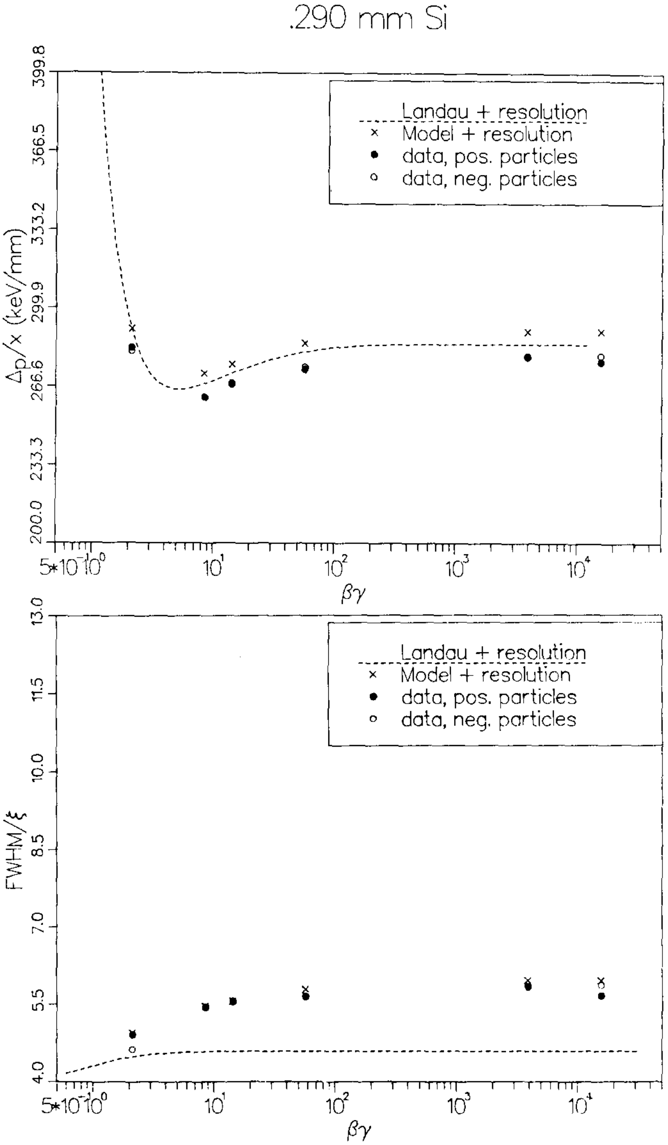

Fig. 18. As fig. 14, but for the 290 μm Si target.

probable energy losses [22, 33]. A reduction in the value of the Fermi plateau, as suggested by Tsytovitch [34], and claimed observed by Zhadanov et al. [35, 36] seems not to have any relevance to the restricted or the most probable energy loss [36, 37]. Also the measurements by Burq et al. [38] do not confirm the predictions of Tsytovitch. Ogle et al. [39] have observed a (7 ± 2)% reduction in the most probable energy loss with respect to the Fermi-plateau for $\gamma \geq 3 \times 10^4$ in a 101 μm Si detector.

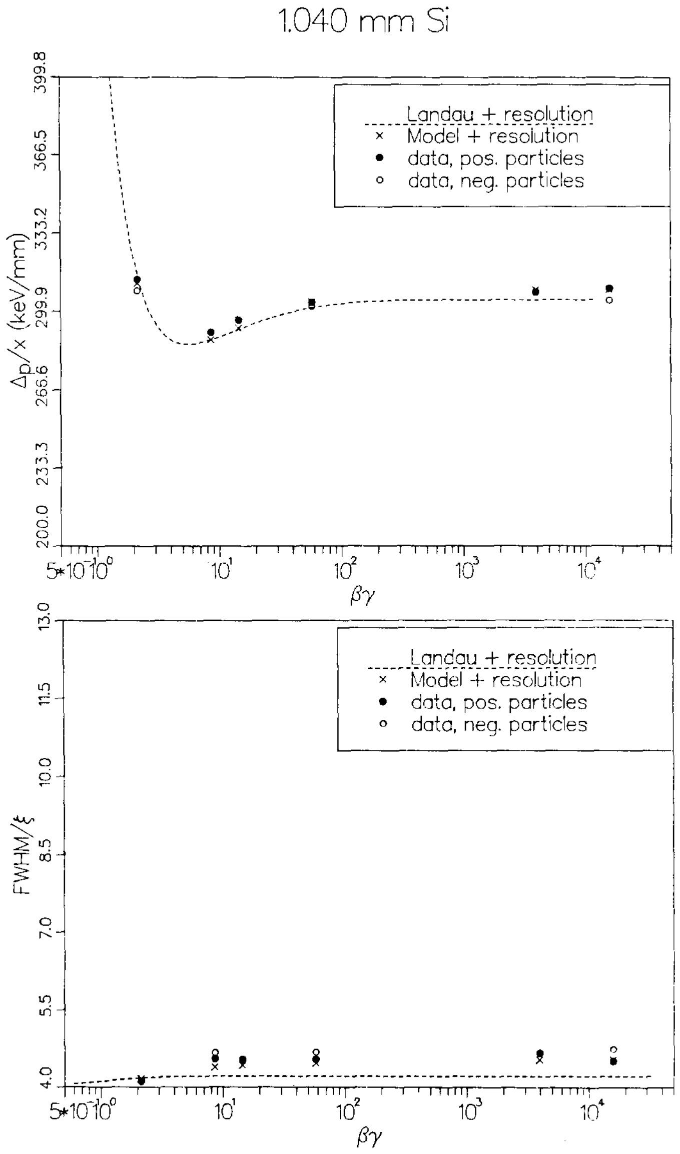

Fig. 19. As fig. 14, but for the 1040 μm Si target.

The authors suggest an explanation in terms of the finite detector thickness and a relativistic effect.

In the present experiment no decrease or increase from the value of the Fermi plateau has been observed for high γ-values. However, this is not in disagreement with the experiment by Ogle et al., since our largest γ-value is 1.6×10^4 for the 174 μm detector and 4×10^3 for the 32.0 μm detector.

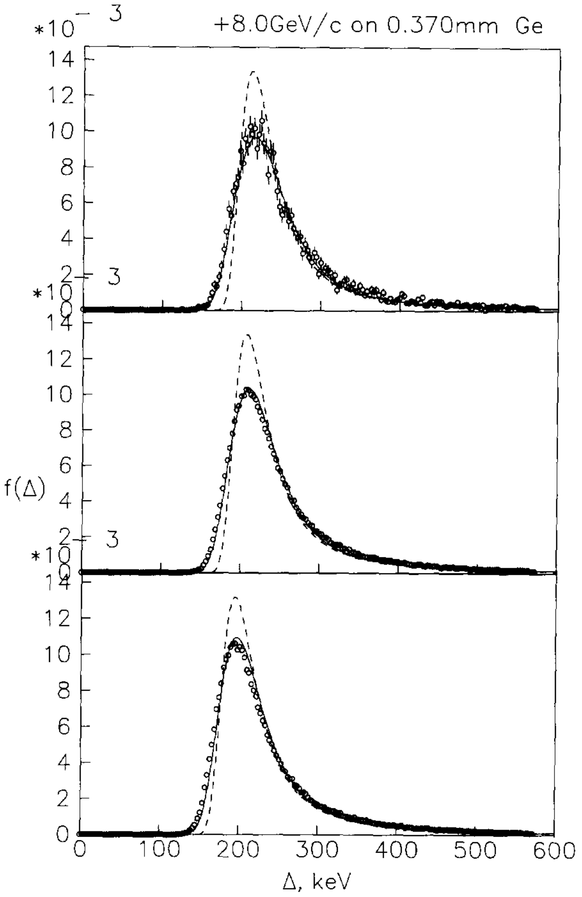

Fig. 20. Experimental energy-loss distributions compared to the Landau function (dashed) and the distribution function from our model (full-drawn). Energy-loss distributions are shown for 8 GeV/c positions (upper part), pions (middle part) and protons (lower part).

5. Concluding remarks

The γ-dependence of the energy loss for relativistic particle impact on solids has been studied in detail. The behaviour of the most probable energy loss as function of $\beta\gamma$ agrees in general well with calculations. In particular, a Fermi plateau constant to within $\sim 1\%$ has been observed over the γ-range covered $C \sim 1$–10^4). Also the observed decrease in the most probable energy loss as function of target thickness is in good agreement with model calculations.

This work represents the first systematic study of energy-loss distributions in solids over a wide range of thicknesses and γ-values. Broadening of the distribution function relative to the Landau function, is observed for decreasing thickness. This broadening is caused by the increasing influence of the resonance collisions on the straggling. The measured energy-loss spectra are generally in good agreement with calculated distribution functions, where the electronical binding effects have been included in the single collision cross section. At the very thinnest targets, discrepancies exist, partly because of experimental problems, partly due to the δ-function representation of the resonance collisions in the cross section. Calculations based on a more realistic energy-loss cross section and better measurements, where particles hitting the edge of the detector are entirely excluded, are needed to investigate the significance of the discrepancies. Finally, the confirmation of the results by Ogle et al. [39] awaits energy loss measurements on foils thinner than 100 μm for γ-values larger than 10^4.

The authors acknowledge valuable discussions with J.U. Andersen, E. Bonderup, J. Lindhard and E. Lægsgård. One of us, (A.B.) expresses his gratitude for the hospitality of the colleagues at the Institute of Physics.

The Danish participation in this work was made possible by funds from the Danish Committee for Accelerator Physics.

References

[1] U. Fano, Ann. Rev. Nucl. Sci. 13 (1963) 1
[2] U. Fano, Phys. Rev. 103 (1956) 1202
[3] W.W.M. Allison and J.H. Cobb, Ann. Rev. Nucl. Part. Sci. 30 (1980) 253
[4] J. Lindhard, Kgl. Danske Vid. Selskab, Mat.-Fys. Medd. 28, no. 8 (1954)
[5] R.M. Sternheimer, Phys. Rev. 88 (1952) 851
[6] L.D. Landau, J. Phys. USSR 8 (1944) 201
[7] O. Blunck and S. Leisegang, Z. Phys. 128 (1950) 500
[8] P. Shulek et al., Sov. J. Nucl. Phys. 4 (1967) 400
[9] G. Hall, Nucl. Instrum. Methods 220 (1984) 356
[10] V.A. Chéchin and V.C. Ermilova, Nucl. Instrum. Methods 136 (1976) 551
[11] S. Hancock et al., Phys. Rev. A28 (1983) 615;
S. Hancock et al., Nucl. Instrum. Methods B1 (1984) 16
[12] K.H. Ispirian et al., Nucl. Instrum. Methods 117 (1974) 125
[13] V.C. Ermilova et al., Nucl. Instrum. Methods 145 (1977) 555
[14] H. Bichsel, Phys. Rev. B1 (1970) 2854; Phys. Rev. A9 (1974) 571;
H. Bichsel and R.P. Saxon, Phys. Rev. A11 (1975) 1286
[15] H. Bichsel, Nucl. Instrum. Methods A235 (1985) 174
[16] J. Lindhard, Physica Scripta 32 (1985) 72
[17] R. Talman, Nucl. Instrum. Methods 159 (1979) 189
[18] R.M. Sternheimer, Phys. Rev. 145 (1966) 247
[19] H.R. Philips and H. Ehrenreich, Phys. Rev. 129 (1963) 1550
[20] F.C. Brown, Solid State Physics 29 (1974) 1
[21] Handbook of Chemistry and Physics (CRC Press, 1973)
[22] S.P. Ahlen, Rev. Mod. Phys. 52 (1980) 121
[23] H. Esbensen et al., Phys. Rev. B18 (1978) 1039
[24] H.D. Maccabee and D.G. Papworth, Phys. Lett. A30 (1969) 241
[25] Average energy required to produce an ion pair, ICRU REPORT 31 (Washington 1979, USA)

[26] U. Fano, Phys. Rev. 72 (1947) 26
[27] S.P. Møller, PhD thesis, University of Aarhus (1986) unpublished
[28] R. Bailey et al., Nucl. Instrum. Methods 213 (1983) 201
[29] C. Julliot and M. Cantin, Nucl. Instrum. Methods 157 (1978) 235
[30] D.W. Aitken et al., Phys. Rev. 179 (1969) 393
[31] J.J. Kolata et al., Phys. Rev. 176 (1968) 484
[32] H.D. Maccabee et al., Phys. Rev. 165 (1968) 469
[33] A. Crispin and G.N. Fowler, Rev. Mod. Phys. 42 (1970) 290
[34] U.N. Tsytovich, Sov. Phys. JETP 16 (1963) 1260
[35] G.D. Zhadanov et al., Sov. Phys. JETP 16 (1963) 245
[36] K.I. Alekseeva et al., Sov. Phys. JETP 17 (1963) 1254
[37] E.G. Drukarev, Sov. J. Nucl. Phys. 33 (1981) 215
[38] J.P. Burq et al., Nucl. Instrum. Methods 187 (1981) 407
[39] W. Ogle et al., Phys. Rev. Lett. 40 (1978) 1242